

Near-Infrared II Nanoadjuvant-Mediated Chemodynamic, Photodynamic, and Photothermal Therapy Combines Immunogenic Cell Death with PD-L1 Blockade to Enhance Antitumor Immunity

Qinyanqiu Xiang, Chao Yang, Yuanli Luo, Fan Liu, Jun Zheng, Weiwei Liu, Haitao Ran, Yang Sun, Jianli Ren, and Zhigang Wang*

The efficacy of immune checkpoint inhibition in inducing death of cancer cells is affected by the immunosuppressive “cold” tumor microenvironment, which results in a poor response by the patient’s antitumor immune system. However, the immunomodulatory effects of immunogenic cell death in response to irritation by heat energy and reactive oxygen species (ROS) can switch the tumor microenvironment from “cold” to “hot.” This study has developed a nanoadjuvant for immune therapy using iron tungsten oxide (FeWO_x)-based nanosheets with surface PEGylation (FeWO_x-PEG). This FeWO_x-PEG nanoadjuvant serves as a chemodynamic reagent via the Fenton reaction and acts as a photosensitizer for photodynamic and photothermal therapy under near-infrared II laser irradiation; however, it could also be used to augment tumor-infiltrating T-cells and provoke a systemic antitumor immune response by combining the immunogenic cell death triggered by ROS and photothermal therapy with the immune checkpoint blockade. This research demonstrates that application of the FeWO_x-PEG nanoadjuvant under the guidance of magnetic resonance/computed tomography/photoacoustic imaging can eliminate the primary tumor and suppress the growth of distant tumors.

demonstrated efficacy against multiple types of cancer by blocking immune evasion of cancer cells using antibodies against programmed cell death 1 (PD-1) and its ligand (PD-L1).^[2] However, monotherapy with ICB has limited clinical potential and benefits only a small number of patients.^[3] The reason for this phenomenon is insufficient infiltration of T cells and a poor immune response, which ultimately results in a less than ideal therapeutic effect.^[4] Therefore, there is an urgent need to find a way of increasing the immune response in patients and achieve more favorable treatment outcomes. One promising strategy would be to trigger immunogenic cell death (ICD), which could transform the immunosuppressive “cold” tumor microenvironment (TME) to an immunoactive “hot” TME by releasing tumor-associated antigens and danger-associated molecular patterns (DAMPs).^[5] A distinct feature of

1. Introduction

Immune checkpoint blockade (ICB) is an emerging anti-tumor strategy that is drawing attention worldwide.^[1] ICB has

ICD, DAMPs augment antigen presentation of dendritic cells, provoking further activation, proliferation, and infiltration of T-cells in the TME.^[5b]

Chemotherapeutics,^[6] photothermal therapy (PTT),^[7] and reactive oxygen species (ROS)-related strategies, including photodynamic therapy (PDT),^[8] sonodynamic therapy (SDT),^[9] and chemodynamic therapy (CDT),^[10] have been established to induce ICD in tumor cells. On the one hand, the ROS-dependent endoplasmic reticulum (ER) stress strategy plays a major role in ICD. The ER, a eukaryotic organelle, responds to oxidative stress induced as a result of overproduction of ROS by activating a complex signaling pathway that further disturbs homeostasis in the ER,^[11] ultimately causing ER stress to become the general “enabler” of ICD. Therefore, methods for augmentation of intracellular ROS for amplification of ICD are actively being sought. CDT uses iron-based nanomaterials to catalyze abnormally high levels of hydrogen peroxide (H₂O₂) in an acidic TME to highly reactive hydroxyl radicals (\cdot OH) via the Fenton reaction,^[12] provoking the ROS production.^[13] In addition, PDT acts as a promising anticancer strategy by converting molecular oxygen into cytotoxic singlet oxygen (¹O₂), which causes cell apoptosis and

Q. Xiang
Department of Radiology
The First Affiliated Hospital of Chongqing Medical University
Chongqing 400010, P. R. China

C. Yang
Department of Radiology
Chongqing General Hospital
University of Chinese Academy of Sciences
Chongqing 400010, P. R. China

Y. Luo, F. Liu, J. Zheng, W. Liu, H. Ran, Y. Sun, J. Ren, Z. Wang
Chongqing Key Laboratory of Ultrasound Molecular Imaging
& Department of Ultrasound
The Second Affiliated Hospital of Chongqing Medical University
Chongqing 400010, P. R. China
E-mail: 303507@hospital.cqmu.edu.cn

 The ORCID identification number(s) for the author(s) of this article can be found under <https://doi.org/10.1002/smll.202107809>.

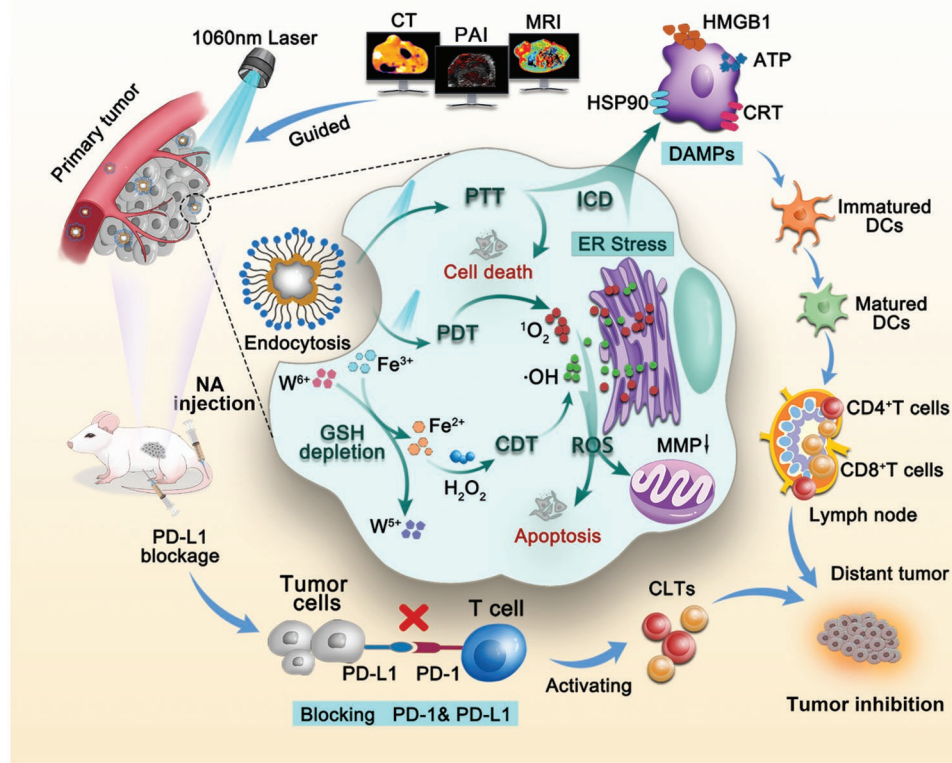
DOI: 10.1002/smll.202107809

further triggers ICD.^[14] Artificially combining CDT and PDT may be a novel strategy for increasing production of ROS. On the other hand, PTT converts optical energy into heat to not only eradicate tumor cells^[15] but also reprogram the immunosuppressive TME by releasing heat shock proteins (HSPs)-related DAMPs, which are known to be essential for inducing ICD.^[16] However, using only one of these two strategies to promote ICD has several shortcomings. Intracellular ROS has a short half-life (10–320 ns) and a short diffusion range (10–55 nm), which results in limited accumulation of ROS and insufficient ER enrichment for satisfactory induction of ER stress.^[17] Meanwhile, PTT is hampered by a lack of irradiation laser power and obvious energy loss in tumor tissue, which results in a poor effect on ICD.^[18] How to reasonably combine the above ICD stimuli is an urgent problem that needs to be solved.

Herein, we report an iron tungsten oxide-based nanoadjuvant (FWO-PEG NA) that can realize CDT/PDT/PTT therapy to eliminate a primary tumor. Use of this nanoadjuvant could allow immunotherapy that combines ROS/PTT cotriggered ICD with ICB antibodies for efficiently inhibiting the growth of distant tumors under laser irradiation at the second near-infrared (NIR)-II biological window. Furthermore, metal tungsten oxide materials ($MxWO_3$, $M = Cs, Rb, Sn$) have strong localized surface plasmon resonance features similar to those of tungsten oxide.^[19] Therefore, FWO-PEG NA holds promise for use in PTT/PDT under NIR-II irradiation. Notably, NIR-II light (1000–1700 nm) can penetrate deeper into tumor tissue (3–5 cm) than

NIR-I light (650–950 nm) to eliminate deep-seated tumors and promote infiltration of T-cells in deep tissue.^[20]

As shown in **Scheme 1**, when the FWO-PEG NA reaches the lysosome via endocytosis, it releases Fe^{2+}/Fe^{3+} , which performs CDT via the Fenton reaction to efficiently produce $\cdot OH$. The FWO-PEG NA successfully produces heat and ROS under 1060 nm light irradiation, ultimately delivering a combination of CDT/PDT/PTT and inducing further ICD in 4T1 breast cancer cells in coordination with antiprogrammed death ligand 1 (anti-PD-L1) antibodies to augment the efficacy of immune therapy. Furthermore, FWO-PEG NA shows a strong ability to deplete glutathione (GSH) as a result of the high valence of Fe^{3+} and W^{6+} ,^[21] which is favorable for enhancement of the ROS level and ER stress-triggered ICD. Given the excellent NIR absorption performance of FWO NS, the nanoadjuvant could act as a photoacoustic (PA) imaging contrast agent for monitoring dynamic changes in tumor structure and function.^[22] Moreover, the Fe and W elements in these nanoadjuvants mean that they have excellent ability of magnetic resonance (MR)^[23] and computed tomography (CT) imaging,^[24] which could guide the therapeutic photoimmune process and lead to further optimization. In summary, based on the above underlying principles, this FWO-PEG NA-mediated CDT/PDT/PTT and ICB combination strategy can be expected to successfully eliminate a primary tumor and strongly suppress progression of distant tumors under multimodal imaging guidance with minimal systemic toxicity.



Scheme 1. Schematic illustration showed FWO-PEG NA mediated CDT/PDT/PTT therapy and antitumor immunity effect amplification via combining ROS/PTT cotriggered ICD with ICB under the PA/CT/MR imaging guidance.

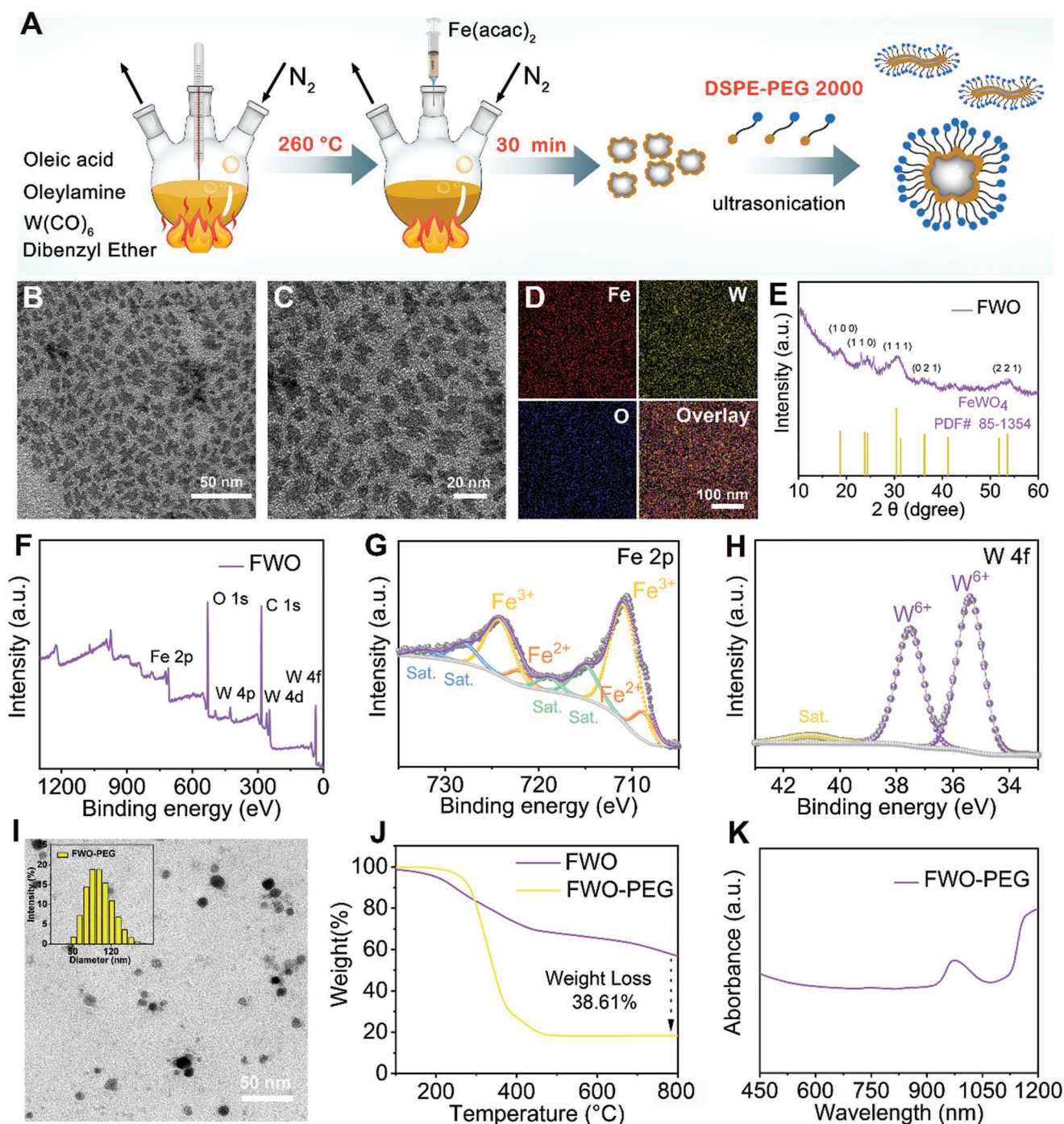


Figure 1. A) Schematic illustration of the synthesis of FWO NS and FWO-PEG NA. B,C) TEM images of FWO NS. D) The corresponding elemental mapping images and E) XRD spectrum of FWO NS. F) XPS survey spectrum and XPS spectra of G) Fe 2p and H) W 4f in FWO NS. I) TEM images of FWO-PEG NA. J) Thermogravimetric analysis (TGA) of FWO NS and FWO-PEG NA. K) Optical UV-vis-NIR absorbance spectrum of the FWO-PEG NA.

2. Results and Discussion

2.1. Characterization of FWO-PEG NA

A typical organic-phase synthesis procedure was performed to synthesize iron tungsten oxide nanosheets (FWO NS)^[25]

as illustrated in **Figure 1A**. Transmission electron microscopy (TEM) images showed that these FWO NS had a lamellar morphology with an average diameter of ≈ 50 nm (**Figure 1B,C**). Line scan energy spectrum analysis (**Figure S1**, Supporting Information) revealed the major elements to be Fe, W, and O, which exhibited a homogeneous distribution in the elemental mapping

images (Figure 1D). As shown in Figure 1E, the natural structure of the FWO NS was explored using X-ray diffraction. The patterns of the FWO NS corresponded to the standard data for FeWO_4 (PDF#851354). The elemental composition of the FWO NS was detected further by X-ray photoelectron spectroscopy, which revealed the coexistence of Fe, W, and O elements in the FWO NS (Figure 1F). The valence state of elements in the FWO NS was assayed further. According to the X-ray photoelectron spectra (Figure 1G, H), the two strong binding energy peaks at 708.80 eV ($\text{Fe}^{2+} 2p_3$) and 722.06 eV ($\text{Fe}^{2+} 2p_1$) corresponded to Fe^{2+} , and the other two peaks located at around 710.91 eV ($\text{Fe}^{3+} 2p_3$) and 724.21 eV ($\text{Fe}^{3+} 2p_1$) were assigned to Fe^{3+} , while the two strong binding energy peaks at 35.40 eV (W 4f7) and 37.54 eV (W 4f5) could be ascribed to W^{6+} . The $\text{Fe}^{2+}/\text{Fe}^{3+}$ ratio was calculated to be approximately 1:2.5. To prepare the PEG-modified FWO-PEG NA, the obtained FWO NS were modified with an amphiphilic polymer (DSPE-PEG 2000) to increase their water solubility (Figure 1A). TEM imaging (Figure 1I) showed that the FWO-PEG NA had a circular-like morphology with a hydrodynamic diameter of 102.57 ± 0.25 nm (polydispersity index 0.08 ± 0.07). The zeta potential of the FWO NS aqueous suspension was -2.23 ± 0.16 mV, which decreased to -14.07 ± 0.40 mV after modification with PEG, further confirming the success of the amphiphilic polymer coating (Figure S2, Supporting Information). In addition, the difference in loss of mass between the two entities detected by thermogravimetric analysis indicated that the proportion of PEG in the FWO-PEG NA was approximately 38.61% (Figure 1J). The ultraviolet-visible of NIR absorbance spectrum (Figure 1K) showed that FWO-PEG NA has absorption peaks around 1000 nm, enabling it to be an efficient absorber for NIR-II activated PTT.

2.2. CDT/PDT/PTT Performance In Vitro

Owing to the unique nanosheet structure of FWO NS, iron atoms are exposed to the greatest extent to the surface, which explains the excellent CDT properties of FWO-PEG NA. Next, 3,3',5,5'-tetramethylbenzidine (TMB) and methylene blue (MB) were used to evaluate the production of $\cdot\text{OH}$. The intermediate $\cdot\text{OH}$ generated could oxidize TMB from colorless to blue with obvious characteristic light absorption at about 652 nm (Figure 2A). Absorption at this wavelength was markedly enhanced in FWO-PEG incubated with H_2O_2 (Figure 2B) and showed an obvious time-dependent trend (Figure 2C and Figure S3, Supporting Information), which indicated that FWO-PEG NA had a favorable CDT effect via the Fenton reaction. In contrast, the production of $\cdot\text{OH}$ could degrade MB gradually from blue to colorless with obvious characteristic light degradation at about 664 nm. As shown in Figure 2D, due to the presence of H_2O_2 and a weak acidic environment, degradation of MB increased the ability of FWO-PEG NA to produce $\cdot\text{OH}$.

According to earlier reports,^[19a,26] WO_3 is a typical n-type semiconductor material, and its high electron transfer reaction is key to its ability to generate ROS under laser irradiation. To confirm that our synthesized FWO-PEG NA also has excellent PDT properties, 1,3-biphenyl isocoumarin-2,5-diphenyl-3,4-benzofuran (DPBF) was used as an indicator to observe the production of $^1\text{O}_2$ initiated by laser irradiation. When DPBF was

oxidized by $^1\text{O}_2$, the color changed from yellow to colorless, with a decreased absorption peak at about 418 nm (Figure 2A). Compared with the insignificant decline in the blank control, laser only, and FWO-PEG groups (Figure S4, Supporting Information), there was a clear time-dependent trend decrease in absorption at approximately 418 nm in the FWO-PEG group under laser irradiation at 1060 nm (Figure 2E and Figure S5, Supporting Information). These findings indicated that our FWO-PEG NA has a PDT effect under NIR-II laser irradiation.

GSH is a core member of the endogenous antioxidant system that prevents ROS,^[27] and consumption of GSH has become a focus of research on ROS-related antitumor strategies.^[28] Because of the high valence states of W^{6+} and Fe^{3+} in the NS, we speculated that our synthesized FWO-PEG NA had a GSH-depleting ability that could be monitored further by the 5,5-dithiobis (2-nitrobenzoic acid) (DTNB) indicators. When incubated with GSH and FWO-PEG NA (Figure 2F and Figure S6, Supporting Information), the characteristic absorption peak of DTNB at about 412 nm decreased markedly as the incubation time increased, confirming that the FWO-PEG NA has an ability to deplete GSH, which could lead to maintenance of a sustainable high ROS level after laser irradiation.

Previous researches^[18,29] has demonstrated that ferric oxide and tungsten oxide nanoparticles (NPs) exhibit high efficiency in PTT in the NIR-II region. Therefore, we investigated whether the synthesized FWO-PEG NA could act as an NIR-II-triggered PTT agent by monitoring the temperature changes using an infrared thermal imaging camera. Under laser irradiation at 1060 nm (1.0 W cm^{-2}) for 5 min, the FWO-PEG NA solution showed concentration-dependent PTT performance as the temperature increased to $48.2 \text{ }^\circ\text{C}$ at a concentration of $400 \mu\text{g mL}^{-1}$ (Figure 2G,H). Furthermore, the highest temperature increase (to $51.3 \text{ }^\circ\text{C}$) occurred when the FWO-PEG NA solution was at a concentration of $400 \mu\text{g mL}^{-1}$ and subjected to laser irradiation at 1.25 W cm^{-2} for 5 min, when an obvious laser power-dependent trend in temperature was observed (Figures S7 and S8, Supporting Information). In addition, upon laser illumination, the temperature did not change significantly after at least five cycles of heating/cooling (Figure S9, Supporting Information), suggesting that the FWO-PEG NA could potentially act as a stable NIR-II-triggered PTT agent for tumor hyperthermia.

2.3. Lysosomal Escape and Intracellular ROS Production

Lysosomal escape and ROS/PTT cotriggered ICD. Lysosomes are formed by continuous division and fusion of a large number of vesicles in an acidic environment (pH 4-5).^[30] As shown in Figure 3A, $\text{Fe}^{3+}/\text{Fe}^{2+}$ was completely released from the FWO-PEG NA and was taken up by cells via endocytosis. The released Fe^{3+} is reduced to Fe^{2+} under the action of a large number of reducing substances (mainly GSH) in lysosomes and occurs when part of the H_2O_2 is dispersed into the lysosome via the Fenton reaction. Production of $\cdot\text{OH}$ leads to peroxidation of the lysosomal membrane, followed by rupture and lysosomal escape of FWO-PEG NA. Consequently, we investigated the intracellular distribution of FWO-PEG NA labeled with DiO. As shown in Figure 3B, after 30 min of incubation, the green fluorescence of DiO from the nanoadjuvant overlapped well with

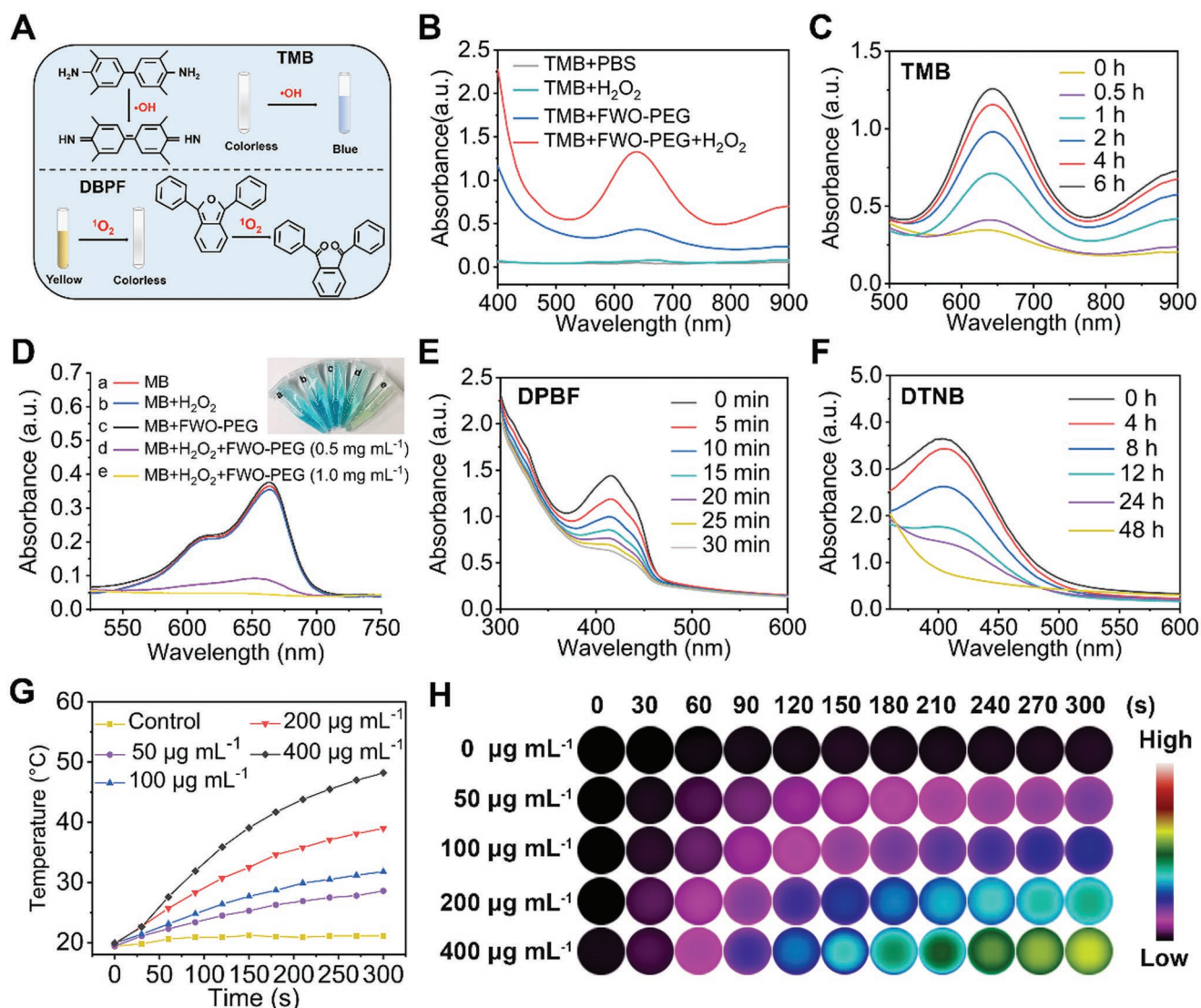


Figure 2. A) Chromogenic principles scheme of TMB and DPBF. B) Comparison of the Fenton reaction effect. C) Time-dependent $\cdot\text{OH}$ generation by FWO-PEG NA, indicating by oxidation of TMB. D) Comparison of MB degradation. E) Time dependent of $^1\text{O}_2$ generation detected via the DPBF probes. F) Time dependent of GSH consumption via DTNB probes. G) Temperature changes of FWO-PEG NA aqueous suspension at different concentrations under NIR-II irradiation (1060 nm, 1.0 W cm⁻²). H) IR thermal images of PBS and FWO-PEG aqueous suspension at different concentrations under NIR-II irradiation (1060 nm, 1.0 W cm⁻²).

the red fluorescence of the lysosome probe (Lyso-Tracker) and was consistent with the findings of the colocalization analysis. Reduced colocalization was observed after 2 h of incubation, suggesting that FWO-PEG NA might escape from the lysosome and enter the cytoplasm where it could exert a further therapeutic effect.

The performance of CDT and PDT *in vitro* was evaluated in view of the aforementioned properties of FWO-PEG NA. The efficiency of production of intracellular $\cdot\text{OH}$ and $^1\text{O}_2$ by the nanoadjuvant was detected using the 2,7-dichlorodihydrofluorescein diacetate (DCFH-DA) probe. As shown in Figure 3C, unlike the control and H_2O_2 groups, the CDT group showed mild green fluorescence signals when the cells were incubated with both FWO-PEG NA and H_2O_2 . Moderate green fluorescence signals were detected in the PDT group when the cells

were incubated with FWO-PEG NA under 1060 nm laser irradiation at 0.5 W cm⁻² for 10 min. It is worth noting that the CDT/PDT group showed strong fluorescence signals, suggested that the highest ROS level in cells could be achieved by combining CDT with PDT. Moreover, the quantitative results obtained by flow cytometry (FCM) analysis corresponded to the above findings observed by confocal laser scanning microscope (CLMS) (Figure 3D).

Furthermore, intracellular ROS can cause mitochondrial dysfunction that could be observed by mitochondrial membrane potential (MMP) using the mitochondrial dye JC-1, which could also characterize cell apoptosis. When the MMP was high and complete, red fluorescence was observed, whereas when it was low or damaged, green fluorescence was seen. As shown in Figure 3C, the CDT group showed bright red fluorescence,

decrease in MMP with an obvious superposition effect. The relative proportions of red and green fluorescence intensity were then detected by FCM (Figure 3E and Figure S10, Supporting Information). Although there were changes in the cells incubated with the nanoadjuvant that were attributed to weak toxicity, there was an obvious decrease in cells incubated with H₂O₂ suggesting that ROS has an ability to produce a decrease in the MMP. Compared with the MMP ratio of 2.4 in the H₂O₂ group, the MMP was reduced to 1.3 in the CDT group and 0.5 in the PDT group. Importantly, MMP in the CDT/PDT group was markedly reduced to 0.3. These results indicate that the CDT/PDT effects of FWO-PEG NA could have a further ROS-related antitumor effect in vivo.

2.4. Immunogenic Cell Death and DCs Maturation in Vitro

In addition to toxicity, the ROS generated can diffuse into the ER and elicit ICD. The location analysis of ROS (Figure S11, Supporting Information) showed the bright green fluorescence from ROS was within the coverage area of red fluorescence (ER-Tracker), which has proved the ROS reached to ER. However, whether the ROS and PTT could trigger ICD, we have investigated DAMPs-related biomarkers. Release of high mobility group box 1 protein (HMGB1), marked overexpression of calreticulin (CRT), secretion of adenosine triphosphate (ATP), and exposure to HSP90 as the characteristic index of DAMPs^[31] was assessed by enzyme-linked immunosorbent assay (ELISA). HMGB1 is a highly conserved chromosomal protein that is released from the nucleus in response to mechanical damage and is considered to be the most representative component of DAMPs.^[32] As shown in Figure 3F, compared with the control group, the HMGB1 levels released were increased by 1.61-fold and 2.03-fold in the CDT/PDT and PTT groups, respectively, which was consistent with the degree of cell damage. CRT is responsible for glycoprotein folding, acts as an “eat me” signal, and can translocate from the ER to the cell surface to assist antigen presentation.^[33] Overexpression of CRT (Figure 3G) was improved by 15.89% in the CDT/PDT group and by 28.32% in the PTT group, which reflected cell apoptosis levels. ATP is secreted by cells undergoing apoptosis, providing a “find me” signal for recruitment of dendritic cells (DCs) and facilitating antigen presentation by these cells.^[11] Our results (Figure 3H) showed that the intracellular ATP level was increased by 1.62-fold after administration of CDT/PDT and by 4.92-fold after administration of PTT. HSP90 belongs to a family of cellular stress proteins that can translocate from the intracellular membrane to the plasma membrane by high-temperature stimulation or other stressful conditions.^[34] Compared with the control group (Figure 3I), the HSP90 level in the CDT/PDT group was slightly increased, which is due to the HSP90 also in response to oxidative stress in PDT.^[35] However, there was significantly higher in the PTT group, indicating the heat energy plays a dominant part in the HSP90 expression. DCs are related to the uptake of antigens, can present antigens to T cells for regulating the antitumor immune response.^[36] Whether the antigens released from ROS/PTT-related ICD could induce the DC maturation in the transwell system was analyzed by FCM (Figure 3J,K). Compared with the control group, the

DC maturation ratio (CD11c⁺ CD86⁺ CD80⁺) in the CDT/PDT group was slightly increased, the PTT group displayed a 1.52-fold higher than control group, which further proved that both the ROS and PTT could activate immune responses in vitro. In summary, FWO-PEG NA could induce ICD efficiently by ROS and PTT and further lead DC maturation for activating antitumor immune responses.

2.5. CDT/PDT/PTT Combination Therapy

A GSH assay kit was used to evaluate the ability of FWO-PEG NA to deplete intracellular GSH. As shown in Figure 4A, GSH levels in the control group remained high but decreased markedly in the group incubated with both H₂O₂ and FWO-PEG. These results suggest that our synthetic nanoadjuvant can deplete intracellular GSH levels efficiently and further magnify the curative effect of ROS-related therapy. Next, we evaluated the therapeutic outcome of CDT/PDT/PTT in vitro. The FWO-PEG NA prepared in PBS showed weak cytotoxicity, and the viability of 4T1 cells was more than 80% even at a concentration of 400 μg mL⁻¹ (Figure S12, Supporting Information). The cytotoxic effects of the various treatments on 4T1 cells were also assessed using the CCK-8 method. As shown in Figure 4B, there was a mild to moderate reduction in cell viability in the groups treated with CDT, PDT, or PTT alone, whereas cell viability was markedly lower in the CPP (CDT/PDT/PTT) group, further suggesting a combination therapeutic effect in vitro. We also performed live/dead cell staining (Figure S13, Supporting Information) and detected cell apoptosis (Figure 4C) in stained 4T1 cells cultured with various treatments to verify the killing effect and found that the CPP group was occupied almost completely by strongly red fluorescent apoptotic cells with an apoptosis rate of 59.26%. These results further confirmed the combination effect of FWO-PEG NA and lay the foundation for in vivo therapy.

The in vivo antitumor effect was investigated (Figure 4D). Typically, as seen in Figure 4E,F, compared with the control group, the temperature in the tumor region under the PTT condition (1.0 W cm⁻², 5 min) increased rapidly to 46.2 °C but was lower at 42 °C under the PDT condition (0.5 W cm⁻², 15 min). The tumor in mouse images (Figure 4I) and volume size (Figure 4G) were monitored after administration of the various treatments. Tumor growth was slightly suppressed in the CDT group but was only moderately inhibited in the CDT/PDT and CDT/PTT groups; noteworthy is that the most obvious tumor inhibition effect occurred in the CPP group. The picture (Figure 4H) and weight of the tumors in vitro (Figure 4I) followed a similar trend, and there was no significant decrease in body weight during the observation period (Figure S14, Supporting Information). Moreover, hematoxylin and eosin (H&E) and immunochemical staining with terminal deoxynucleotidyl transferase-mediated dUTP nick-end labeling (TUNEL) and proliferating cell nuclear antigen (PCNA) (Figure 4J) were performed to observe the histological features of the tumor tissue. We could see from the H&E-stained tumor slices that there was almost a full field of deformed nuclei and apoptosis in the CPP group, which was consistent with the results of the TUNEL assay. Moreover, the PCNA assay showed almost no proliferative

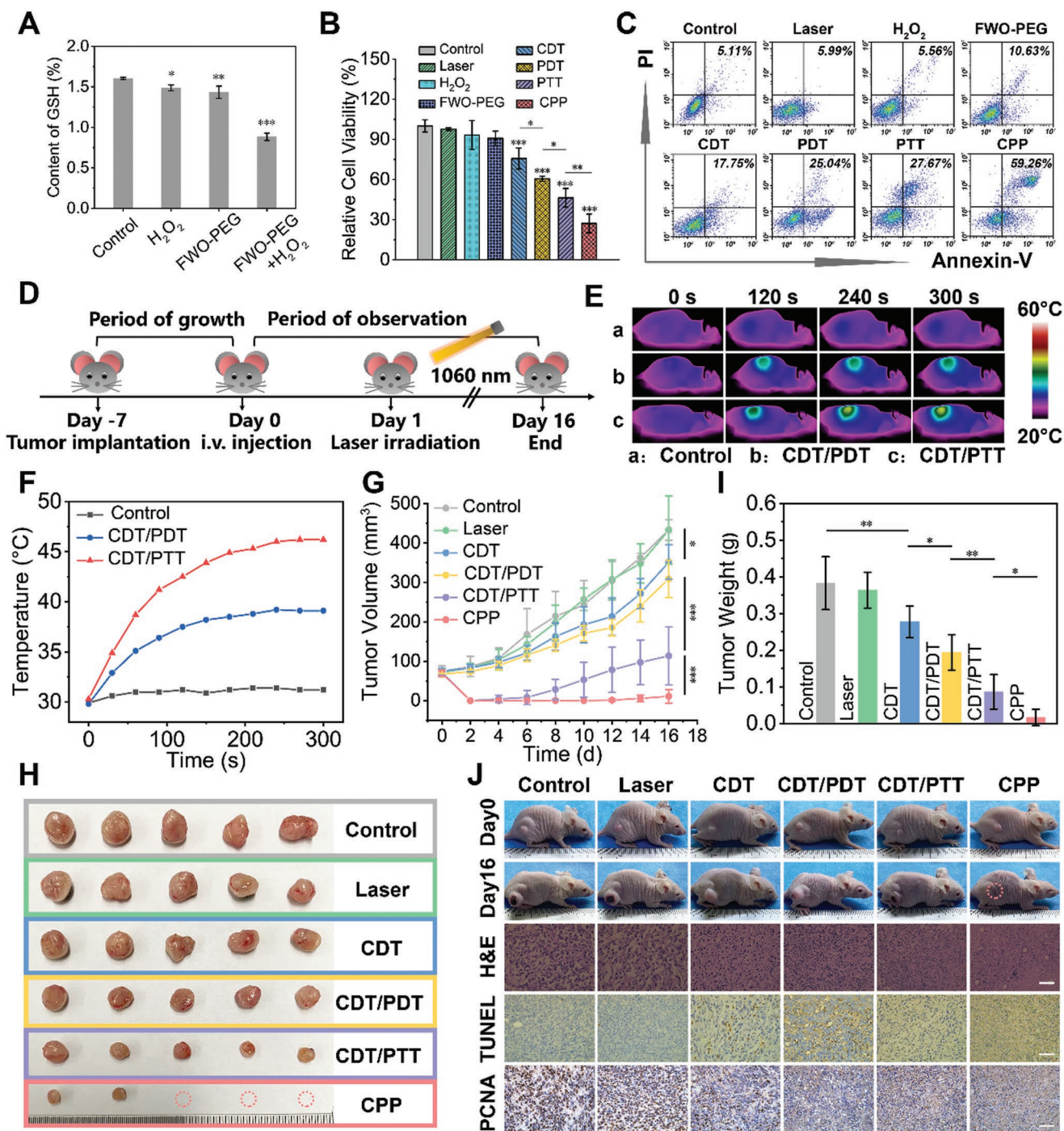


Figure 4. A) Intracellular GSH level after different treatments ($n = 3$). B) Relative cell viability of cells after different treatments. 1. Control; 2. Laser; 3. H₂O₂; 4. FWO-PEG; 5. CDT (FWO-PEG + H₂O₂); 6. PDT (FWO-PEG + 0.5 W cm⁻² × 10 min); 7. PTT (FWO-PEG + 1.0 W cm⁻² × 5 min); 8. CPP (CDT/PDT/PTT: FWO-PEG + H₂O₂ + 0.5 W cm⁻² × 10 min + 1.0 W cm⁻² × 5 min) ($n = 3$). C) Apoptosis quantified of the corresponding groups by FCM analysis. D) Schematic illustration of the FWO-PEG NA for primary tumor on female BALB/c-nude mice. E) The corresponding IR thermal images and F) temperature changes at tumor regions of the three groups. G) Tumor volume changes of six groups after various treatments ($n = 5$). H) Photographs of tumors dissected from mice of six groups after various treatments. I) Weight of tumors 16 days post various treatments ($n = 5$). J) Photographs of mice of six groups at day 0/day 16 and H&E/TUNEL/PCNA immunochemical staining of tumor sections after various treatments. Scale bar: 50 μ m. * $p < 0.05$, ** $p < 0.01$, *** $p < 0.001$.

activity in the CPP group. These results indicate that the FWO-PEG NA-mediated CDT/PDT/PTT therapy was characterized by a favorable therapeutic outcome when compared with the other

treatments. The safety of FWO-PEG NA was evaluated by collecting the major organs from mice in each treatment group on the day following irradiation. H&E staining of the organs

did not reveal any detectable histopathological abnormalities (Figure S15, Supporting Information).

2.6. PA/CT/MRI and the Biodistribution/Metabolism of FWO-PEG NA

Photoacoustic imaging has considerable potential for clinical use because of its high spatial resolution and nonionizing radiation.^[14] When we set the excitation wavelength to 680 nm, the FWO-PEG NA showed the obvious photoacoustic intensity in the range of 680–970 nm (Figure S16, Supporting Information). The photoacoustic signal of the nanoadjuvant in vitro was clearly dose-dependent and showed a prominent linear relationship (Figure 5A), showing an increase from 0.23 to 0.89 with increasing concentration. For in vivo photoacoustic imaging (Figure 5B), there was a significant photoacoustic signal in the tumor region after injection of FWO-PEG NA, which was consistent with the quantitative analysis (Figure 5C). Overall, our FWO-PEG NA showed good photoacoustic imaging properties that could provide more biomolecular information at the tumor site for future applications. CT imaging allows rapid scanning and has powerful computer postprocessing functions with better positioning of lesions.^[37] As shown in Figure 5D, the CT signal of FWO-PEG NA was noticeably dose-dependent with a good linear relationship, increasing to 268.4 HU at a concentration of 4 mg mL⁻¹. After injection with the nanoadjuvant in vivo, a bright CT signal was seen in the region of the tumor (Figure 5E); the signal reached 141 HU (Figure 5F), confirming that FWO-PEG NA could be used as an effective CT contrast agent. MRI has the advantages of high resolution, being non-radioactive, and obtaining multiple imaging sequences, so is an important diagnostic imaging modality.^[38] We further investigated the performance of MRI and the field-dependent magnetization hysteresis of FWO-PEG NA and demonstrated the superparamagnetic nature of the nanoadjuvant at a temperature of 300 K (Figure S17, Supporting Information). T1-weighted MRI contrast images in vitro (Figure 5G) showed that the images became brighter with increasing concentration, suggesting that the FWO-PEG NA has the significant paramagnetic properties. For in vivo application, as shown in Figure 5H, T1-weighted MRI of the tumor site became brighter 2 h after intravenous administration of FWO-PEG NA. T1 mapping also showed effective accumulation of the nanoadjuvant at the tumor site, where the signal intensity after administration of FWO-PEG NA was 1.6-fold higher than that in the control group (Figure 5I). These findings suggest that FWO-PEG NA has the potential to be a high-sensitivity T1 contrast agent for MRI.

The blood circulation time and nanoadjuvant content in the major organs were assessed by inductively coupled plasma-optical emission spectroscopy (ICP-OES) to determine the biodistribution and metabolism of FWO-PEG NA. As shown in Figure 5J, the circulation half-life was calculated to be 1.38 h, which provides the necessary conditions for good biosafety of the nanoadjuvant in vivo. The biodistribution assay showed that FWO-PEG NA preferentially accumulated in the liver, lung, and spleen rather than in the tumor at 2 h postinjection; when the time was prolonged to 24 h, accumulation in the liver, lung, and spleen was markedly reduced whereas the decrease

was only slight in tumors and lower only than the level in the liver (Figure 5K). Rapid clearance from the blood and organs indicates that FWO-PEG NA can be used safely as a nanotherapeutic reagent for imaging and treatment in vivo (Figure 5L).

2.7. Combination of ROS/PTT Triggered ICD and Anti-PD-L1 for Enhancement of Immune Therapy

Having established that both ROS-dependent ER stress and PTT cotriggered ICD responses in vitro, we assessed whether the combined ICD and anti-PD-L1 strategy could promote an immune response against distant tumors (Figure 6A). Figure 6B shows that CPP (CDT/PDT/PTT) and CPPA (CDT/PDT/PTT/Anti-PD-L1) eliminated tumor growth at the primary site, which was expected. The distant tumor growth (Figure 6C and Figure S18, Supporting Information) was slightly suppressed in the anti-PD-L1, CDT, and CDT/PDT groups and moderately inhibited in the CPP group under stimulation of ICD triggered by ROS and PTT. It is noteworthy that growth of distant tumors was markedly suppressed when CPPA was combined with FWO-PEG NA-mediated ICD intervention and ICB therapy. This finding confirms that the antitumor immune effect was significantly enhanced when synergistic ICD and ICB immunotherapy were applied. Negligible fluctuation in mouse body weight was observed in all of the study groups during the treatment period (Figure S19, Supporting Information), indicating the safety of these interventions.

To further elucidate the mechanisms underlying the superior tumor-suppressive efficacy, we assessed the response of immune cells to distant tumors (Figure 6D). CD8⁺ T-cells are the main effector cells of the tumor immune response and can directly destroy 4T1 breast cancer cells by inducing formation of perforin and effector molecules. CD4⁺ T-cells are mainly expressed by T-helper cells and can release cytokines to assist in tumor immunity.^[39] Consistent with the trend of restriction of distant tumor growth, fewer CD8⁺ and CD4⁺ T-cells were observed in the single treatment group compared with the control group, but were present in significantly higher numbers in the CPP group (14.56% and 12.72%, respectively) and the CPPA group (20.32% and 19.00%) than in the other groups. It is noteworthy that although there were both antitumor immunization effects in the CPP and CPPA groups, the CPPA group showed the highest proliferative activity of T cells. This finding suggests that combined treatment with ICB and FWO-PEG NA-mediated ROS/PTT co-triggered ICD could amplify activation of the immune antitumor response.

After the various treatments, the tumor tissue was subjected to immunofluorescent staining to assess the damage to the tumors and the immune response levels. The trend of damage to the primary tumors observed with TUNEL (green fluorescence) was consistent with the level of inhibition in the primary tumors, and both groups showed extensive damage with a large area of bright green fluorescence (Figure 7A). Moreover, we found that the tumor-infiltrating CD8⁺ and CD4⁺ T-cells in the CPPA group showed the greatest proliferation in distant tumors (Figure 7A). Compared with the control group, medium-intensity fluorescence was observed in the CPP group with little fluorescence in the other groups, indicating that

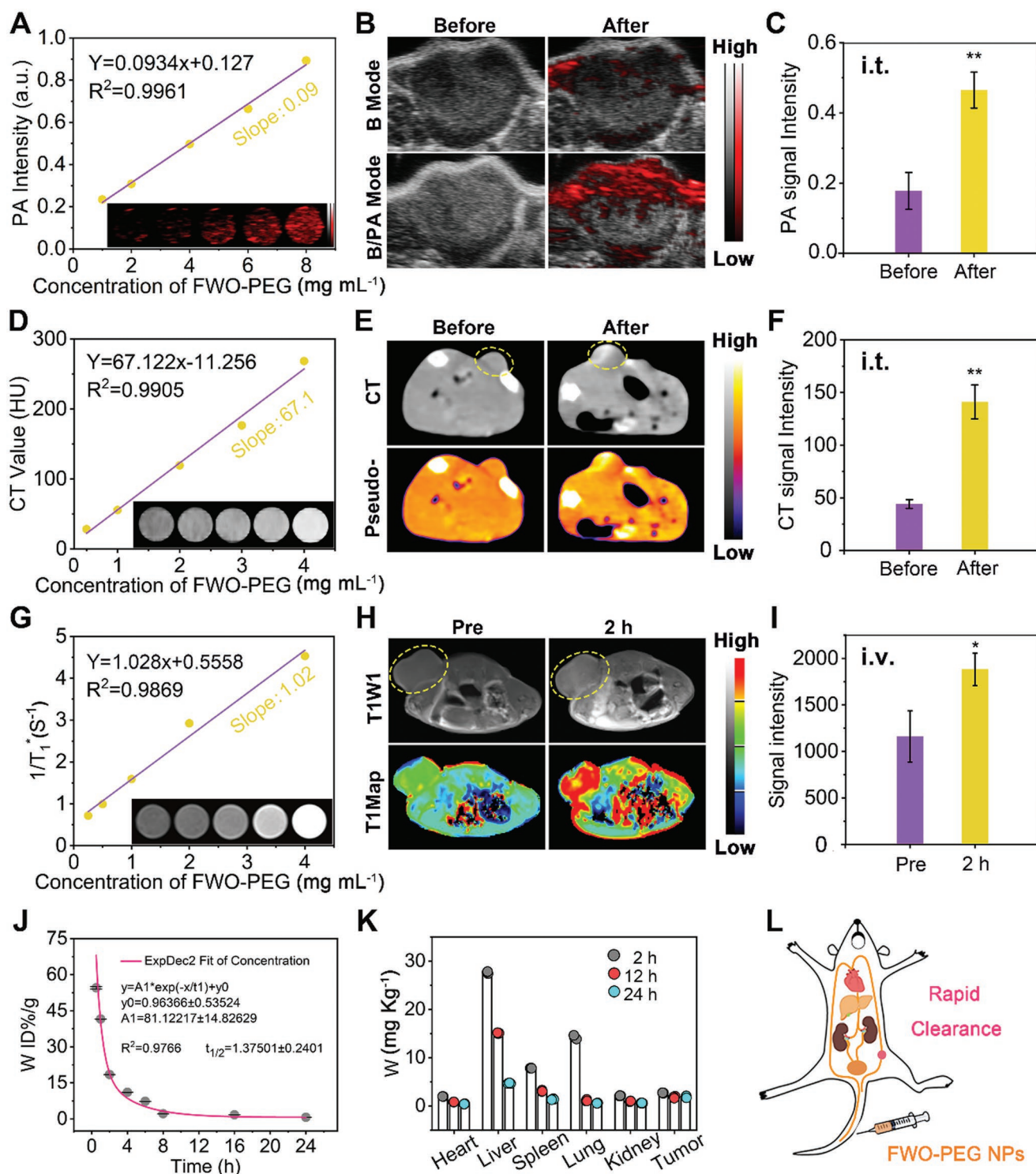


Figure 5. A) In vitro PA contrast images and PA values of FWO-PEG NA at different concentrations. B) In vivo PA images of tumors before and after intratumoral (i.t.) injection of FWO-PEG NA. C) PA-signal intensities within tumor regions ($n=3$). D) CT contrast images and CT values of FWO-PEG NA at different concentrations in vitro. E) CT images and pseudocolored images of tumors before and after i.t. injection of FWO-PEG NA. F) The CT-signal intensities of tumor regions before and after i.t. injection ($n=3$). G) MR images of FWO-PEG NA at different concentrations and the relative T1 relaxation rates. H) T1-weighted and T1-mapping MR images recorded at tumor region after intravenous (i.v.) injection of FWO-PEG NA at different time points. I) Quantification of MR signals of tumor regions ($n=3$). J) The blood-circulation time of administrated FWO-PEG NA is determined by ICP-OES. K) Quantitative biodistribution of FWO-PEG NA in mice determined by ICP-OES at different times. L) Schematic illustration of the rapid body clearance of FWO-PEG NA. * $p < 0.05$, ** $p < 0.01$, *** $p < 0.001$.

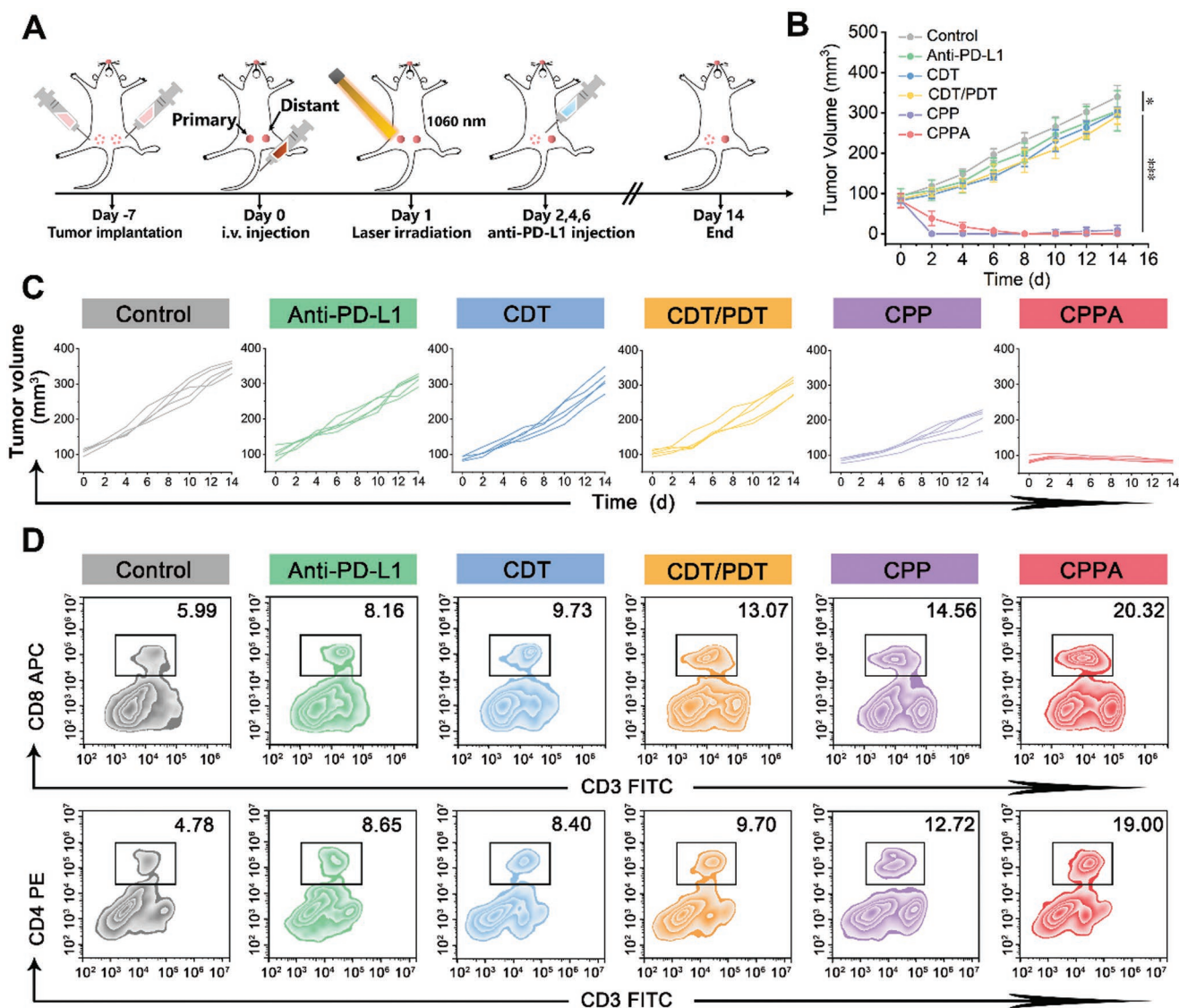


Figure 6. A) Schematic diagram of combining FWO-PEG NA with anti-PD-L1 strategy for inhibiting distant tumor on female BALB/c mice. B) Tumor volume changes of the primary tumor after various treatments. 1. Control; 2. Anti-PD-L1; 3. CDT (FWO-PEG); 4. CDT/PDT (FWO-PEG + $0.5 \text{ W cm}^{-2} \times 15 \text{ min}$); 5. CPP (CDT/PDT/PTT: FWO-PEG + $0.5 \text{ W cm}^{-2} \times 15 \text{ min} + 1.0 \text{ W cm}^{-2} \times 5 \text{ min}$); 6. CPPA (CDT/PDT/PTT/Anti-PD-L1: FWO-PEG + $0.5 \text{ W cm}^{-2} \times 15 \text{ min} + 1.0 \text{ W cm}^{-2} \times 5 \text{ min} + \text{Anti-PD-L1}$) ($n = 5$). C) Tumor volume changes of the distant tumor in six groups after various treatments. D) FCM analysis of CD4⁺/CD8⁺ T-cells expression of tumors. * $p < 0.05$, ** $p < 0.01$, *** $p < 0.001$.

FWO-PEG NA-mediated ICD could work reasonably efficiently in coordination with ICB to promote proliferation of tumor-infiltrating T-cells, causing further suppression of the growth of distant tumors.

As shown in Figure 7B–E, both the CPP and CPPA groups had significantly higher serum expression levels of interleukin (IL)-6, IL-12, tumor necrosis factor (TNF)- α , and interferon (IFN)- γ , all of which are biomarkers released by immune cells, after the strong immune response was triggered. However, the CPPA group showed the highest levels of immune markers, which further demonstrated that FWO-PEG NA mediated thermal ablation, that ROS dual-induced ICD effectively triggered the immune response, and further synergistic ICB amplified the systemic immune response to suppress distant tumors.

Finally, we investigated the biosafety of FWO-PEG NA. The blood biochemistry indices (Figure 7F) did not indicate any toxicity in mice at the tested dose in the short term or longer term. Moreover, there were no significant histopathological changes in the major organs at the tested doses (Figure 7G), indicating no toxicity in mice, further establishing the potential clinical application of this nanoadjuvant.

3. Conclusion

In this study, FWO-PEG NA was synthesized via a high-temperature organic-phase procedure and was used as a novel Fenton reagent and phototherapeutic sensitizer in the treatment of

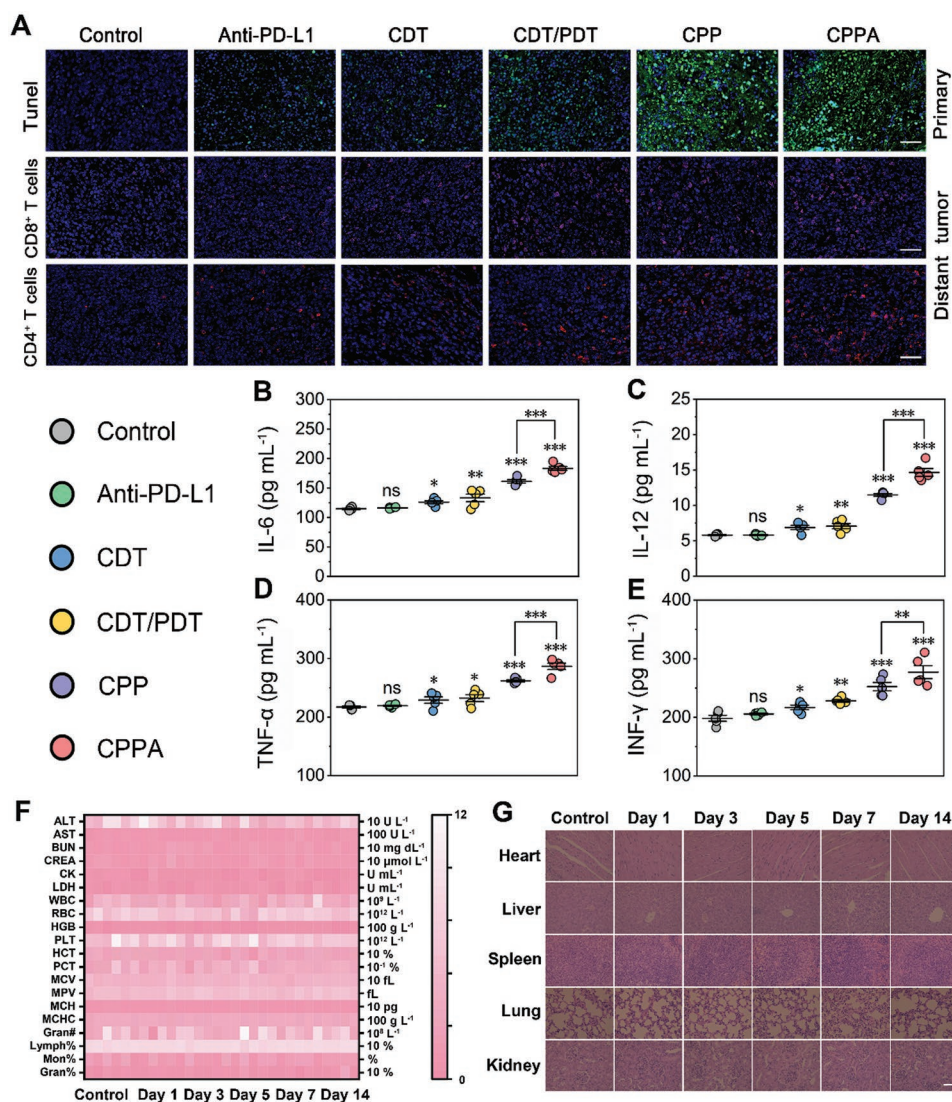


Figure 7. A) Immunofluorescence staining of TUNEL on the primary tumor and immunofluorescence staining of CD4⁺/CD8⁺ T-cells on the distant tumor. Scale bar: 50 μm . B–E) The level of IL-6, IL-12, TNF- α , and IFN- γ in serum of different groups by ELISA ($n = 5$). F) Hematological and blood biochemical test of mice after i.v. administration of FWO-PEG NA at different time intervals. G) H&E staining of the major organs at corresponding time intervals. Scale bar: 50 μm . * $p < 0.05$, ** $p < 0.01$, *** $p < 0.001$.

tumors. This nanoadjuvant was demonstrated to not only generate toxic $\cdot\text{OH}$ by reaction with H_2O_2 in the tumor TME but also induce robust generation of ROS and heat energy under NIR-II laser activation with strong depletion of GSH. Importantly, upon application of external stimulation by NIR-II, CDT/PDT and PTT-related ICD could trigger DC maturation to activate T-cells-related antitumor immune responses and work in concert with ICB treatment by reversing the immunosuppressive TME and promoting antitumor immunogenicity. In vivo animal experiments showed that FWO-PEG NA had a combination CDT/PDT/PTT effect in the primary tumor elimination and the synergistic ICD/ICB immunotherapy can strongly inhibit the distant tumors based on monitoring by photoacoustic imaging, CT, and MRI. These findings suggest that FWO-PEG NA is a new effective immunomodulatory strategy that works by amplification of ICD and enhancing the response to ICB immunotherapy.

4. Experimental Section

Reagents: Hexacarbonyl tungsten, 5,5-dithiobis (2-nitrobenzoic acid) (DTNB), and 1,3-biphenyl isocoumarin-2,5-diphenyl-3,4-benzofuran (DPBF) were purchased from Sigma-Aldrich (St Louis, MO, USA). Ferrrous acetylacetonate and 3,3',5,5'-tetramethylbenzidine (TMB) were obtained from Aladdin Reagent Ltd., Co. (Shanghai, China). Benzyl ether and 1,2-dodecanediol were purchased from TCI Development Co., Ltd. (Shanghai, China). Antimouse PD-L1 was purchased from Bio X Cell (Beijing, China). All immunoassay-related fluorescent antibodies were purchased from BioLegend, Inc. (California, USA).

Synthesis of FWO Nanosheets: Briefly, 20 mL of benzyl ether, 1.5 g of 1,2-dodecanediol, and 1 mmol of hexacarbonyl tungsten were loaded into a three-necked flask under nitrogen gas flow with vigorous magnetic stirring. Next, the system temperature was increased to 120 $^\circ\text{C}$ and 1 mL of oleic acid and 1 mL of oleylamine were added to the system. The temperature was then increased to 260 $^\circ\text{C}$, and 1 mmol of ferrous acetylacetonate was injected into the mixture. After maintaining this temperature for 30 min, the mixture was cooled to room temperature

and centrifuged at 13 000 rpm for 10 min with cyclohexane and excess anhydrous ethanol to obtain FeWO_x nanosheets (FWO NS).

Transfer of FWO NS to an Aqueous Phase: Typically, 10 mg of FWO NS and 40 mg of DSPE-PEG 2000 each in 2 mL of chloroform were mixed and subjected to ultrasonication for 30 min. The mixture was then stirred for 2 h, followed by drying with nitrogen gas. Finally, the iron tungsten oxide-based nanoadjuvant (FWO-PEG NA) was washed with deionized water for later use.

Characterization: The morphology and structure of the FWO-PEG NA were determined using a Tecnai G2 F30 transmission electron microscope (FEI Company, Hillsboro, OR, USA) and an Xplore energy-dispersive X-ray spectroscope (Oxford Instruments, Abingdon, UK). Zeta potentials were measured by dynamic light scattering (Malvern Instruments, Malvern, UK). Powder X-ray diffraction analysis was carried out using a PANalytical X'Pert Powder X-ray diffractometer (Spectris Netherlands B.V., Almelo, Netherlands). X-ray photoelectron spectroscopy measurements were obtained using the Escalab 250Xi platform (Thermo Fisher Scientific, Waltham, MA, USA). Optical absorption was determined using an ultraviolet-visible spectrophotometer (US-2550, Shimadzu, Tokyo, Japan). Thermogravimetric analysis was performed using a TGA/DSC1/1600LF instrument (Mettler Toledo, Zurich, Switzerland). Inductively coupled plasma-optical emission spectroscopy analysis was performed using an iCAP 6300 Duo system (Thermo Fisher Scientific).

Detection of Hydroxyl Radicals: The ability of the FWO-PEG NA to generate hydroxyl radical ($\cdot\text{OH}$) was detected by TMB. Briefly, 4 μL of TMB ($80 \times 10^{-3} \text{ M}$) were injected into 1 mL of FWO-PEG NA ($500 \mu\text{g mL}^{-1}$). The changes in absorbance of TMB at 652 nm were observed at reaction times of 0, 0.5, 1, 2, 4, and 6 h. Generation of $\cdot\text{OH}$ via the Fenton reaction was also indicated by the degree of degradation of methylene blue (MB) observed by ultraviolet-visible spectroscopy. Solutions of phosphate-buffered saline (PBS; pH 6.0) containing 10 $\mu\text{g mL}^{-1}$ methylene blue and $1 \times 10^{-3} \text{ M H}_2\text{O}_2$ with FWO-PEG NA (the FWO-PEG NA group) or without FWO-PEG NA (the laser only group) were prepared.

Detection of Singlet Oxygen: Generation of singlet oxygen ($^1\text{O}_2$) was determined using DPBF. First, 20 μL of DPBF (1 mg mL^{-1}) were injected into 1 mL of FWO-PEG NA ($500 \mu\text{g mL}^{-1}$), and the system was subjected to laser irradiation at 1060 nm (0.5 W cm^{-2}) with monitoring of the changes in absorption at 418 nm after 0, 5, 10, 15, 20, 25, and 30 min. The laser only and FWO-PEG groups were compared.

Depletion of Glutathione: Depletion of glutathione (GSH) was detected by ultraviolet-visible spectroscopy. FWO-PEG NA ($500 \mu\text{g mL}^{-1}$) was dissolved in 1 mL of PBS and reacted with $1 \times 10^{-3} \text{ M GSH}$. Next, 6 μL of DTNB (10 mg mL^{-1}) were added, and the changes in absorption in the mixture at 412 nm were measured after 1 min of reaction after 0, 4, 8, 12, 24, and 48 h.

Photothermal Properties In Vitro: The photothermal properties of FWO-PEG NA were evaluated at concentrations of 50, 100, 200, and 400 $\mu\text{g mL}^{-1}$ after laser irradiation at 1060 nm (1.0 W cm^{-2}). FWO-PEG NA ($400 \mu\text{g mL}^{-1}$) was also irradiated at power densities of 0.25, 0.5, 0.75, 1.0, and 1.25 W cm^{-2} . PBS was used as the control solution.

Cell Culture: Murine 4T1 breast cancer cells were cultured in a humidified atmosphere with 5% CO_2 at 37 °C and grown in RPMI 1640 medium (Hyclone, Thermo Scientific, USA) containing 10% fetal bovine serum and 1% penicillin-streptomycin (v/v).

Lysosomal Escape: 4T1 cells were inoculated into cell culture dishes for 24 h at a density of 1×10^5 per dish. Next, the cells were incubated in fresh RPMI 1640 medium containing DiO-labeled FWO-PEG NA ($400 \mu\text{g mL}^{-1}$). After incubation for 30 min or 2 h, all dishes were washed with PBS, fixed with 4% formaldehyde for 15 min, and stained with DAPI and LysoTracker-Red (Beyotime Biotechnology, Shanghai, China) for 10 or 30 min, respectively. All dishes were examined using a confocal laser scanning microscope (CLSM; Nikon A1+R, Tokyo, Japan). Colocalization analysis was performed using ImageJ software (National Institutes of Health, Bethesda, MD, USA).

Detection of Intracellular ROS/JC-1: Briefly, cells were seeded in cell culture dishes at a density of 1×10^5 cells per dish and incubated for 24 h. The medium was then replaced with fresh medium containing

either PBS, H_2O_2 ($100 \times 10^{-6} \text{ M}$), or FWO-PEG NA ($400 \mu\text{g mL}^{-1}$). The solutions were then incubated for a further 4 h. Two cell groups were formed: a CDT group, which was treated with FWO-PEG NA and H_2O_2 , and a PDT group, which was exposed to 1060 nm laser irradiation (0.5 W cm^{-2}) for 10 min after incubation with FWO-PEG NA. Next, all cells were stained with DCFH-DA for detection of ROS. The cells were also stained with JC-1 dye to observe variations in the mitochondrial membrane potential (MMP). All dishes were imaged by CLSM, and cells were collected for flow cytometry (FCM) analysis (BD FACSVantage SE, BD Biosciences, Franklin Lakes, NJ, USA). MMP was calculated as the ratio of the JC-1 aggregate/monomer.

Cellular ROS Localization: Cells were seeded in dishes at a density of 1×10^5 cells per dish and incubated for 24 h. The cells were then incubated with FWO-PEG NA ($400 \mu\text{g mL}^{-1}$) for 4 h. The cells were then exposed to irradiation at 1060 nm (0.5 W cm^{-2}) for 10 min. After fixing for 15 min with 4% formaldehyde, the cells were stained with DAPI for 10 min and ER-TrackerRed (Beyotime Biotechnology) for 30 min. All dishes were imaged by CLSM. The colocalization analysis was performed using ImageJ software.

Immunogenic Cell Death Induced by FWO-PEG NA In Vitro: Cells were seeded in six-well plates at a density of 2×10^5 cells per well. Cells in the CDT/PDT groups were incubated with H_2O_2 ($100 \times 10^{-6} \text{ M}$) and FWO-PEG NA ($400 \mu\text{g mL}^{-1}$) and cells in the PTT group were incubated with FWO-PEG NA ($400 \mu\text{g mL}^{-1}$), both for 4 h. After incubation, cells in the CDT/PDT group were exposed to 1060 nm laser irradiation (0.5 W cm^{-2}) for 10 min and those in the PTT group was exposed to 1060 nm laser irradiation (1.0 W cm^{-2}) for 5 min. After a further 2 h of incubation, the cell supernatants were collected to detect immunogenic cell death-related HSP90, CRT, HMGB1, and ATP levels using the HSP90, CRT, and HMGB1 ELISA kits (Enzyme Free Industrial Co., Ltd, Jiangsu, China), and the ATP assay kit (Beyotime Biotechnology), respectively.

DC Stimulation Experiment In Vitro: The transwell system was used to coculture 4T1 cells and DCs. Typically, residual 4T1 cells were took different treatments and put in upper layer plate of the system, while the DCs were seeded in the lower layer and for 24 h coincubation. Then, single-cell suspensions were stained with anti-CD11c-APC anti-CD80-FITC, and anti-CD86-PE for FCM analysis. Four treatment groups were created: Control (DCs + 4T1 cells); Laser (DCs + 4T1 cells treated with laser); CDT/PDT (DCs + 4T1 cells treated with H_2O_2 and laser irradiation at 0.5 W cm^{-2} for 10 min); PTT (DCs + 4T1 cells treated with laser irradiation at 1.0 W cm^{-2} for 5 min).

Detection of Cell GSH Levels: Cell GSH levels were assessed using a GSH assay kit (Beyotime Biotechnology). Cells were seeded at a density of 2×10^5 per well in six-well plates and incubated for 24 h, followed by 4 h incubation with PBS, H_2O_2 ($100 \times 10^{-6} \text{ M}$), or FWO-PEG NA ($400 \mu\text{g mL}^{-1}$). Finally, the cell GSH levels were detected according to the manufacturer's protocol.

Animals and Tumor Models: Female BALB/c nude mice and BALB/c mice were purchased from Tengxin Biotechnology Co., Ltd (Chongqing, China) and housed at the Experimental Animal Center at Chongqing Medical University. All experiments and procedures were performed in accordance with the guidelines of the Institutional Animal Care and Use Committee. The tumor volumes were calculated as $0.5 \times \text{length} \times \text{width}^2$.

In Vitro Antitumor Efficacy: The CCK-8 method was used to detect cell viability in the experimental groups after the various treatments. First, the safety of the FWO-PEG NA was assessed. 4T1 cells were seeded in a 96-well plate at a density of 1×10^4 cells per well. After incubation for 24 h, various concentrations of the nanoadjuvant were added. After a further 24 h of incubation, cell viability was measured. In the CDT group, the antitumor activity of FWO-PEG NA was assessed further by culturing the cells with FWO-PEG NA ($400 \mu\text{g mL}^{-1}$) and H_2O_2 ($100 \times 10^{-6} \text{ M}$) and incubation for 4 h. Cells were incubated with FWO-PEG NA and subjected to 1060 nm laser irradiation (0.5 W cm^{-2}) for 10 min (PDT group) or 1.0 W cm^{-2} for 5 min (PTT group). The CPP group received CDT/PDT/PTT combination therapy. After these treatments, cell viability was measured using the CCK-8 assay. Live-dead cell staining was also used to assess antitumor efficacy in vitro. Cells from each group were also evaluated for apoptosis using FCM.

Photoacoustic Imaging: The photoacoustic performance of FWO-PEG NA was assessed using a Vevo LAZR imaging system (Visual Sonics Inc., Toronto, ON, Canada). To determine the excitation wavelength, the maximum absorbance of the FWO-PEG NA was measured from 680 to 970 nm. Next, photoacoustic imaging was performed at different concentrations of FWO-PEG NA (1, 2, 4, 6, and 8 mg mL⁻¹) and the corresponding photoacoustic signal was monitored. For in vivo photoacoustic imaging, intratumoral injections of FWO-PEG NA in saline solution (4 mg mL⁻¹, 200 µL) were administered to tumor-bearing mice ($n = 3$) and the photoacoustic signal of the tumor region was measured using the built-in software.

CT Imaging: The computed tomography (CT) imaging performance of FWO-PEG NA was assessed using a clinical CT imaging system (Siemens Medical Systems, Erlangen, Germany) at Chongqing General Hospital. The CT signal calibration curve was assessed using different concentrations of FWO-PEG NA (0.5, 1, 2, 3, and 4 mg mL⁻¹) in PBS. The imaging parameters were set at 120 kV and 80 kV. For CT imaging in vivo, 4T1 tumor-bearing mice ($n = 3$) were injected intratumorally with FWO-PEG NA (4 mg mL⁻¹, 200 µL) in saline solution and pseudocolor images were created using ImageJ software.

MR Imaging Performance: The ability of MR imaging to capture accurate images of FWO-PEG NA in vitro and in vivo was assessed using the corresponding T1 relaxation times obtained using the Siemens 3-T MRI system at The Second Affiliated Hospital of Chongqing Medical University. First, the MRI signal calibration curve was created by detection of several concentrations of FWO-PEG NA (0.25, 0.5, 1, 2, and 4 mg mL⁻¹) in saline solution. The performance of MR imaging in vivo was then evaluated further using MR images acquired from tumor-bearing mice ($n = 3$) 2 h after they had received intravenous injections of FWO-PEG NA saline solution (4 mg mL⁻¹, 200 µL).

Biodistribution Study: The metabolism of FWO-PEG NA was investigated in blood samples collected from BALB/c mice at 2, 12, and 24 h after intravenous administration of FWO-PEG NA (4 mg mL⁻¹, 200 µL). The mice were then euthanized, and the major organs (heart, liver, spleen, lung, and kidney) and tumors were collected. All samples were subjected to inductively coupled plasma-optical emission spectroscopy to obtain the W mass in each sample (% ID/g).

CDT/PDT/PTT Antitumor Therapy In Vivo: The effects of CDT, PDT, and PTT on the primary tumors were then estimated in vivo. A 4T1 tumor-bearing nude mouse model was established by subcutaneous injection of 4T1 cells (1×10^6) dispersed in 100 µL of PBS per mouse in female BALB/c-nude mice. Six treatment groups were created: control (group 1); laser (group 2); CDT (group 3); CDT/PDT (group 4); CDT/PTT (group 5); CPP (CDT + PDT + PTT; group 6). On day 0, FWO-PEG NA (4 mg mL⁻¹, 200 µL) in saline solution was intravenously injected into mice in the experimental groups and saline solution only was injected in the control group. Twenty-four hours later, mice in groups 4 and 6 underwent 1060 nm laser irradiation at 0.5 W cm⁻² for 15 min and mice in groups 2, 5, and 6 underwent 1060 nm laser irradiation at 1.0 W cm⁻² for 5 min. For photothermal imaging, temperature and infrared thermal images were captured in groups 1, 4, and 5 using an infrared thermal imaging camera (Fotric 226; Wenzhou Valvespro Flow Control Technology Co., Ltd. Zhejiang, China). Mouse body weight and tumor diameters were recorded on alternate days for 16 d. On day 3, tumors and major organs were collected from one mouse in each group for histological evaluation with hematoxylin-eosin (H&E) staining. Proliferation of tumors was assessed with proliferating cell nuclear antigen (PCNA) and terminal deoxynucleotidyl transferase dUTP nick end (TUNEL) staining.

Combined ICD/ICB Immunotherapy: To evaluate the effect of immunogenic cell death and immune checkpoint blockade therapy on distant tumor, each BALB/c female mouse was subcutaneously inoculated with a cell suspension (1×10^6) under the left and right breast to create the primary tumor and distant tumor, respectively. 4T1 tumor-bearing mice were randomly divided into six groups: control (group 1); anti-programmed death ligand 1 (Anti-PD-L1; group 2); CDT (group 3); CDT/PDT (group 4); CPP (CDT + PDT + PTT; group 5); and CPPA (CDT + PDT + PTT + Anti-PD-L1; group 6). The mice in groups

4, 5, and 6 were intravenously injected with FWO-PEG NA on day 0. Twenty-four hours later, the primary tumors in group 4 were subjected to laser irradiation at 1060 nm (0.5 W cm⁻²) for 15 min and the primary tumors in groups 5 and 6 were subjected to laser irradiation at 1060 nm with both 0.5 W cm⁻² for 15 min and 1.0 W cm⁻² for 5 min, respectively. The mice in groups 2 and 6 were injected intraperitoneally with anti-PD-L1 (1.0 mg kg⁻¹ per mouse) on days 2, 4, and 6. During the 14 days of observation, body weight and tumor diameters were recorded on alternate days.

The left-sided (primary) tumors in all groups were collected and subjected to immunofluorescence staining with TUNEL on day 3. On day 7, the mice were euthanized to obtain blood samples. Serum was collected from each mouse to detect levels of interleukin (IL)-6, IL-12, TNF- α , and IFN- γ by ELISA (Enzyme Immune). The right-sided (distant) tumors in all groups were collected and digested with 0.2% collagenase D, 0.01% hyaluronidase, and 0.002% DNase (Solarbio, Beijing, China) for 30 min at 37 °C. All cells were then filtered through 40 µm cell filters and washed with PBS. Finally, single-cell suspensions were stained with anti-CD3-FITC, anti-CD8-APC, and anti-CD4-PerCP for FCM analysis. On day 7, the right-sided (distant) tumors were collected, and tissue sections were subjected to the CD4⁺ and CD8⁺ T-cells immunofluorescence staining.

Biosafety: To estimate the toxicity of FWO-PEG NA in vivo, FWO-PEG NA (4 mg mL⁻¹, 200 µL) or saline solution was intravenously injected into BALB/c mice, who were then randomly divided into six groups (1, 3, 5, 7, and 14 d postinjection), with noninjected mice serving as the control group. All major organs and blood samples were collected for testing.

Statistical Analysis: All data are expressed as the mean \pm standard deviation. One-way analysis of variance and the Student's *t*-test were used to test the significance of differences among groups. All statistical analyses were performed using SPSS software (version 22.0; IBM Corp., Armonk, NY, USA). A *p*-value <0.05 was considered statistically significant.

Supporting Information

Supporting Information is available from the Wiley Online Library or from the author.

Acknowledgements

This work was supported by the National Natural Science Foundation of China (No. 82172092) and Chongqing Science & Technology Commission (No. cstc2019jcsx-dxwtBX0004).

Conflict of Interest

The authors declare no conflict of interest.

Data Availability Statement

Research data are not shared.

Keywords

immune checkpoint blockade, immunogenic cell death, iron tungsten oxide, multimodal imaging, multimodal theranostics

Received: December 16, 2021
Published online:

- [1] a) D. Zhang, Z. Lin, M. Wu, Z. Cai, Y. Zheng, L. He, Z. Li, J. Zhou, L. Sun, G. Chen, Y. Zeng, J. Li, J. Liu, H. Yang, X. Liu, *Adv. Sci.* **2021**, 8, 2003504; b) C. Sun, R. Mezzadra, T. N. Schumacher, *Immunity* **2018**, 48, 434.
- [2] a) W. Sang, L. Xie, G. Wang, J. Li, Z. Zhang, B. Li, S. Guo, C. X. Deng, Y. Dai, *Adv. Sci.* **2021**, 8, 2003338; b) M. Konstantinidou, T. Zarganes-Tzitzikas, K. Magiera-Mularz, T. A. Holak, A. Domling, *Angew. Chem., Int. Ed. Engl.* **2018**, 57, 4840.
- [3] Y. Mi, C. T. t. Hagan, B. G. Vincent, A. Z. Wang, *Adv. Sci.* **2019**, 6, 1801847.
- [4] L.-P. Zhao, R.-R. Zheng, J.-Q. Huang, X.-Y. Chen, F.-A. Deng, Y.-B. Liu, C.-Y. Huang, X.-Y. Yu, H. Cheng, S.-Y. Li, *ACS Nano* **2020**, 14, 17100.
- [5] a) L. Jin, S. Shen, Y. Huang, D. Li, X. Yang, *Biomaterials* **2021**, 268, 120582; b) D. V. Krysko, A. D. Garg, A. Kaczmarek, O. Krysko, P. Agostinis, P. Vandenabeele, *Nat. Rev. Cancer* **2012**, 12, 860.
- [6] J. Liu, Z. Zhao, N. Qiu, Q. Zhou, G. Wang, H. Jiang, Y. Piao, Z. Zhou, J. Tang, Y. Shen, *Nat. Commun.* **2021**, 12, 2425.
- [7] a) Z. Yang, D. Gao, X. Guo, L. Jin, J. Zheng, Y. Wang, S. Chen, X. Zheng, L. Zeng, M. Guo, X. Zhang, Z. Tian, *ACS Nano* **2020**, 14, 17442; b) H. Tang, X. Xu, Y. Chen, H. Xin, T. Wan, B. Li, H. Pan, D. Li, Y. Ping, *Adv. Mater.* **2021**, 33, 2006003.
- [8] Z. Wang, X. Gong, J. Li, H. Wang, X. Xu, Y. Li, X. Sha, Z. Zhang, *ACS Nano* **2021**, 15, 5405.
- [9] X. Jiao, L. Sun, W. Zhang, J. Ren, L. Zhang, Y. Cao, Z. Xu, Y. Kang, P. Xue, *Biomaterials* **2021**, 272, 120787.
- [10] B. Ding, P. Zheng, F. Jiang, Y. Zhao, M. Wang, M. Chang, P. Ma, J. Lin, *Angew. Chem., Int. Ed. Engl.* **2020**, 59, 16381.
- [11] Z. Dai, J. Tang, Z. Gu, Y. Wang, Y. Yang, Y. Yang, C. Yu, *Nano Lett.* **2020**, 20, 6246.
- [12] Z. Tang, Y. Liu, M. He, W. Bu, *Angew. Chem., Int. Ed. Engl.* **2019**, 58, 946.
- [13] a) Q. Chen, L. Liu, Y. Lu, X. Chen, Y. Zhang, W. Zhou, Q. Guo, C. Li, Y. Zhang, Y. Zhang, D. Liang, T. Sun, C. Jiang, *Adv. Sci.* **2019**, 6, 1802134; b) B. Li, G. Hao, B. Sun, Z. Gu, Z. P. Xu, *Adv. Funct. Mater.* **2020**, 30, 1909745.
- [14] Q. Xiang, B. Qiao, Y. Luo, J. Cao, K. Fan, X. Hu, L. Hao, Y. Cao, Q. Zhang, Z. Wang, *Theranostics* **2021**, 11, 1953.
- [15] a) B. Qiao, Y. Luo, H. B. Cheng, J. Ren, J. Cao, C. Yang, B. Liang, A. Yang, X. Yuan, J. Li, L. Deng, P. Li, H. T. Ran, L. Hao, Z. Zhou, M. Li, Y. Zhang, P. S. Timashev, X. J. Liang, Z. Wang, *ACS Nano* **2020**, 14, 12652; b) Y. Luo, B. Qiao, P. Zhang, C. Yang, J. Cao, X. Yuan, H. Ran, Z. Wang, L. Hao, Y. Cao, J. Ren, Z. Zhou, *Theranostics* **2020**, 10, 6987.
- [16] W. Li, J. Yang, L. Luo, M. Jiang, B. Qin, H. Yin, C. Zhu, X. Yuan, J. Zhang, Z. Luo, Y. Du, Q. Li, Y. Lou, Y. Qiu, J. You, *Nat. Commun.* **2019**, 10, 3349.
- [17] H. Deng, Z. Zhou, W. Yang, L. S. Lin, S. Wang, G. Niu, J. Song, X. Chen, *Nano Lett.* **2020**, 20, 1928.
- [18] Z. Liu, X. Zhao, B. Yu, N. Zhao, C. Zhang, F. J. Xu, *ACS Nano* **2021**, 15, 7482.
- [19] a) W. Guo, C. Guo, N. Zheng, T. Sun, S. Liu, *Adv. Mater.* **2017**, 29, 1604157; b) G. Tian, X. Zhang, X. Zheng, W. Yin, L. Ruan, X. Liu, L. Zhou, L. Yan, S. Li, Z. Gu, Y. Zhao, *Small* **2014**, 10, 4160; c) Y. Gao, F. Wang, W. Huang, C. Yang, W. Guo, C. Song, Q. Zhang, B. Yang, Y. Xu, C. Guo, *Nanoscale* **2019**, 11, 3300.
- [20] a) Y. Jiang, J. Huang, C. Xu, K. Pu, *Nat. Commun.* **2021**, 12, 742; b) J. Li, X. Yu, Y. Jiang, S. He, Y. Zhang, Y. Luo, K. Pu, *Adv. Mater.* **2021**, 33, 2003458; c) W. Liu, H. Xiang, M. Tan, Q. Chen, Q. Jiang, L. Yang, Y. Cao, Z. Wang, H. Ran, Y. Chen, *ACS Nano* **2021**, 15, 6457.
- [21] a) J. Shen, T. W. Rees, Z. Zhou, S. Yang, L. Ji, H. Chao, *Biomaterials* **2020**, 251, 120079; b) Y. Yong, C. Zhang, Z. Gu, J. Du, Z. Guo, X. Dong, J. Xie, G. Zhang, X. Liu, Y. Zhao, *ACS Nano* **2017**, 11, 7164.
- [22] F. Gong, N. Yang, Y. Wang, M. Zhuo, Q. Zhao, S. Wang, Y. Li, Z. Liu, Q. Chen, L. Cheng, *Small* **2020**, 16, 2003496.
- [23] Z. Tang, H. Zhang, Y. Liu, D. Ni, H. Zhang, J. Zhang, Z. Yao, M. He, J. Shi, W. Bu, *Adv. Mater.* **2017**, 29, 1701683.
- [24] Y. Cheng, F. Yang, G. Xiang, K. Zhang, Y. Cao, D. Wang, H. Dong, X. Zhang, *Nano Lett.* **2019**, 19, 1179.
- [25] F. Gong, L. Cheng, N. Yang, Q. Jin, L. Tian, M. Wang, Y. Li, Z. Liu, *Nano Lett.* **2018**, 18, 6037.
- [26] L. Wen, L. Chen, S. Zheng, J. Zeng, G. Duan, Y. Wang, G. Wang, Z. Chai, Z. Li, M. Gao, *Adv. Mater.* **2016**, 28, 5072.
- [27] I. Gusarov, I. Shamovsky, B. Pani, L. Gautier, S. Eremina, O. Katkova-Zhukotskaya, A. Mironov, A. Makarov, E. Nudler, *Nat. Commun.* **2021**, 12, 4336.
- [28] H. Lei, X. Wang, S. Bai, F. Gong, N. Yang, Y. Gong, L. Hou, M. Cao, Z. Liu, L. Cheng, *ACS Appl. Mater. Interfaces* **2020**, 12, 52370.
- [29] L. Sun, Z. Li, R. Su, Y. Wang, Z. Li, B. Du, Y. Sun, P. Guan, F. Besenbacher, M. Yu, *Angew. Chem., Int. Ed. Engl.* **2018**, 57, 10666.
- [30] J. P. Luzio, P. R. Pryor, N. A. Bright, *Nat. Rev. Mol. Cell Biol.* **2007**, 8, 622.
- [31] S. D. Jeong, B. K. Jung, H. M. Ahn, D. Lee, J. Ha, I. Noh, C. O. Yun, Y. C. Kim, *Adv. Sci.* **2021**, 8, 2001308.
- [32] M. M. Lou, X. Q. Tang, G. M. Wang, J. He, F. Luo, M. F. Guan, F. Wang, H. Zou, J. Y. Wang, Q. Zhang, M. J. Xu, Q. L. Shi, L. B. Shen, G. M. Ma, Y. Wu, Y. Y. Zhang, A. B. Liang, T. H. Wang, L. L. Xiong, J. Wang, J. Xu, W. Y. Wang, *Nat. Commun.* **2021**, 12, 4075.
- [33] M. Obeid, T. Panaretakis, A. Tesniere, N. Joza, R. Tufi, L. Apetoh, F. Ghiringhelli, L. Zitvogel, G. Kroemer, *Cancer Res.* **2007**, 67, 7941.
- [34] F. H. Schopf, M. M. Biebl, J. Buchner, *Nat. Rev. Mol. Cell Biol.* **2017**, 18, 345.
- [35] M. E. Rodriguez, I. S. Cogno, L. S. Milla Sanabria, Y. S. Moran, V. A. Rivarola, *Photochem. Photobiol. Sci.* **2016**, 15, 1090.
- [36] Y. Lu, F. Xu, Y. Wang, C. Shi, Y. Sha, G. He, Q. Yao, K. Shao, W. Sun, J. Du, J. Fan, X. Peng, *Biomaterials* **2021**, 278, 121167.
- [37] N. J. Serkova, K. Glunde, C. R. Haney, M. Farhoud, A. De Lille, E. F. Redente, D. Simberg, D. C. Westerly, L. Griffin, R. P. Mason, *Cancer Res.* **2021**, 81, 1189.
- [38] R. S. Campbell, A. J. Grainger, I. G. Hide, S. Papastefanou, C. G. Greenough, *Skeletal Radiol.* **2005**, 34, 63.
- [39] A. M. van der Leun, D. S. Thommen, T. N. Schumacher, *Nat. Rev. Cancer* **2020**, 20, 218.